Supplemental Material for: Floquet control of optomechanical bistability in multimode systems

Karl Pelka,[1] Guilhem Madiot,[2] Rémy Braive,[2,3,4] and André Xuereb[1]

[1]*Department of Physics, University of Malta, Msida MSD 2080, Malta*
[2]*Centre de Nanosciences et de Nanotechnologies, CNRS, Université Paris-Saclay, Palaiseau, France*
[3]*Université de Paris, F-75006 Paris, France*
[4]*Institut Universitaire de France, Paris, France*

(Dated: July 18, 2022)

I. CORRECTIONS TO THE POWER SPECTRAL DENSITY OF HIGHER-ORDER FLOQUET MODES

The experimentally recorded spectra show additional imbalance of the modulation sidebands which cannot be explained in terms of the leading order description. Therefore, we inspect the linearized fluctuation dynamics

$$\begin{aligned}\dot{\hat{\mathfrak{a}}} &= -\left(i\Delta + \frac{\kappa}{2}\right)\hat{\mathfrak{a}} - i\sum_{j=1}^{N} g_j\left(\alpha\Re(\hat{\mathfrak{b}}_j) + \hat{\mathfrak{a}}\mathrm{R}(\beta_j)\right) + \sqrt{\kappa}\hat{\mathfrak{a}}_{\mathrm{in}},\\ \dot{\hat{\mathfrak{b}}}_j &= -\left(i\Omega_j + \frac{\Gamma_j}{2}\right)\hat{\mathfrak{b}}_j - ig_j(\alpha^*\hat{\mathfrak{a}} + \alpha\hat{\mathfrak{a}}^\dagger) + \sqrt{\Gamma_j}\hat{\mathfrak{b}}_{j,\mathrm{in}}. \qquad (1)\end{aligned}$$

The periodic mean field $\alpha(t) = \sum_n \bar{\alpha}_n e^{-in\Omega_{\mathrm{mod}}t}$ allows to expand the fluctuation dynamics in terms of Floquet modes

$$\begin{aligned}\dot{\hat{\mathfrak{a}}}^{(m)} =& -\chi_m^{-1}\hat{\mathfrak{a}}^{(m)} - \sum_{(p,q)}\sum_{j=1}^{N}\chi^{-1}_{\mathrm{OM},jq}\bar{\alpha}_p\bar{\alpha}^*_{p-q}\hat{\mathfrak{a}}^{(m-q)}\\ &- \sum_{n=-D}^{D}\sum_{j=1}^{N} ig_j\bar{\alpha}_{-n}\Re(\hat{\mathfrak{b}}_j^{(m-n)}) + \sqrt{\kappa}\hat{\mathfrak{a}}^{(m)}_{\mathrm{in}},\\ \dot{\hat{\mathfrak{b}}}_j^{(m)} =& -\tilde{\chi}^{-1}_{\mathrm{me},m}\hat{\mathfrak{b}}_j^{(m)} - ig_j\sum_{n=-D}^{D}(\bar{\alpha}^*_{-n}\hat{\mathfrak{a}}^{(m-n)} + \bar{\alpha}_n\hat{\mathfrak{a}}^{\dagger(m-n)})\\ &+ \sqrt{\Gamma_j}\hat{\mathfrak{b}}^{(m)}_{j,\mathrm{in}}, \qquad (2)\end{aligned}$$

with $\tilde{\chi}^{-1}_{\mathrm{me},m} = i(\Omega_j - m\Omega_{\mathrm{mod}}) + \Gamma_j/2$. Restricting to $\hat{\mathfrak{a}}^{(0)}$ results in Eq. (5) in the main text. Including the higher order fluctuation modes results in the Fourier transform

$$\hat{\mathfrak{a}}^{(0)}(\omega) = \frac{\sqrt{\kappa}\hat{\mathfrak{a}}^{(0)}_{\mathrm{in}}(\omega) - \sum\limits_{p=-D}^{D}\sum\limits_{j=1}^{N}\frac{ig_j\bar{\alpha}_p\sqrt{\Gamma_j}\hat{\mathfrak{b}}^{(p)}_{j,\mathrm{in}}(\omega)}{\chi^{-1}_{\mathrm{me},-p} - i\omega}}{\chi^{-1}_{0,\mathrm{cav}} - i\omega + \sum\limits_{p=-D}^{D}\sum\limits_{j=1}^{N}|\bar{\alpha}_p|^2\chi^{-1}_{\mathrm{OS},pj}(\omega)} \qquad (3)$$

which shows that the optomechanical interaction alters the optical detuning and decay rate by $\chi^{-1}_{\mathrm{OS},pj} = \chi^{-1}_{\mathrm{OM},j0} + \chi^{-1}_{\mathrm{OM},j}(\omega + p\Omega_{\mathrm{mod}})$ where the former contribution is frequency independent and leads to the static optical spring effect covered in the main text. The latter contributions however make the effective detuning $\tilde{\Delta}(\omega) = \bar{\Delta} + \sum_{j,p}|\bar{\alpha}_p|^2\mathrm{Im}(\chi^{-1}_{\mathrm{OM},j}(\omega + p\Omega_{\mathrm{mod}}))$ and decay $\tilde{\kappa}(\omega) = \kappa + \sum_{j,p}2|\bar{\alpha}_p|^2\mathrm{Re}(\chi^{-1}_{\mathrm{OM},j}(\omega + p\Omega_{\mathrm{mod}}))$ frequency dependent which will also be reflected in the accessible power spectral density of the output field

$$S(\omega) = \tilde{S} + \sum_{p,j}\frac{\kappa g_j^2|\bar{\alpha}_p|^2\Gamma_j\bar{n}_j}{\left[(\omega - \tilde{\Delta})^2 - \frac{\tilde{\kappa}^2}{4}\right]\left[(\omega - \Omega_{jp})^2 + \frac{\Gamma_j^2}{4}\right]}. \qquad (4)$$

These effects modify the cavity density of states and lead to a change of the apparent imbalance of the mean field amplitudes $|\alpha_n|^2$ displayed by the power spectral density. These contributions were not included in the numerical analysis of the experiment as they made the numerical fitting procedure unstable.

II. THERMO-OPTIC EFFECT AND THERMALIZATION TIME

The physical origin of the thermo-optic effect in our experiment is the temperature growth in the material induced by light absorption which is responsible for a significant shift of the dielectric index, the elastic properties, and consequently the cavity geometry. In an optical cavity, this effect is enhanced such that it can red-shift the cavity resonance frequency. If the input field intensity passes a certain threshold, the resonance lineshape becomes bistable. Such behavior can be evidenced by scanning forward and backward the laser frequency over the resonance, or equivalently, by sweeping up and down the input laser intensity.

We use a tunable laser and inject light into the waveguide through the aligned injection fibers. The output laser field is sent to a low-power photodetector and the DC response is checked on an oscilloscope. Therefore, the waveguide transmission is now triggered in real-time, provided that the transmission can be re-normalized. The input power is estimated by measuring the off-resonance transmission $\zeta \approx 0.1$ of the integrated waveguide and assuming the injection and the collection efficiency to be equal. The input power is therefore $P_{\mathrm{in}} = \sqrt{\zeta}P_{\mathrm{inj}}$ with the optical power sent in the injection fiber P_{inj}. For low power the observed transmission dip can be fitted with the linear transmission expression such that the internal and external Q-factors are determined. In Fig. 1 (a), with $P_{\mathrm{in}} = 325\ \mu$W, we find $Q_i \approx 4400$ and $Q_{\mathrm{w}} \approx 9500$. This corresponds to the internal loss rate of $\kappa_i \approx 2\pi \times 43.3$ GHz and external loss rate of $\kappa_w \approx 2\pi \times 20.2$ GHz. The measurement is reproduced using both forward and backward scans of the laser wavelength at $P_{\mathrm{in}} \approx 1.3$ mW. We fit the

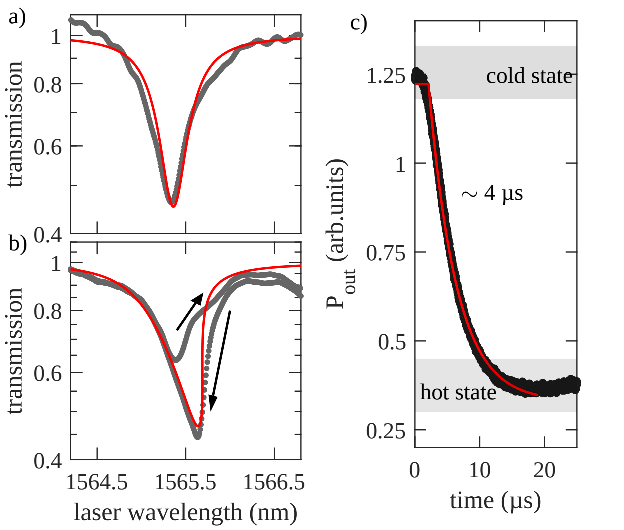

FIG. 1. a) Spectral transmission response using CW laser with input power $P_{\mathrm{in}} \approx 325$ μW. The data (grey dots) are fitted with a CMT model (red line). b) Idem using $P_{\mathrm{in}} \approx 1.3$ mW. Here both forward and backward scans evidence an hysteretic behaviour due to thermo optic nonlinearity. c) Averaged dynamical response of the photonic mode under 10 kHz square modulation of the input laser set to the bistability center. Measurements (black dots) are fitted with ring-down and built-in exponential functions (red) returning a heating time of 4.4 μs.

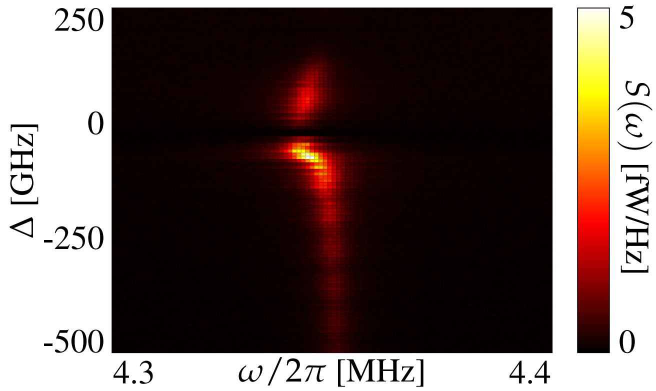

FIG. 2. Experimental output spectrum of the cavity for varying detuning Δ with $P_{\mathrm{in}} = 325\mu$W. As the drive approaches resonance the mechanical frequency is minimal which can be attributed to the decrease of elastic moduli of InP.

data with a nonlinear CMT model implementing a linear dependence of the resonance wavelength with the cavity temperature. Although the fit accurately matches with the width of the observed dip, and also retrieves the presence of a bistable region, we note a disagreement in the size of the bistability. We attribute this discrepancy to a too large scanning speed of the laser wavelength. In practice, it is set at 10 nm/s in order to prevent oscillations in the laser output power, which would have corrupted the measured transmission. This results in an averaging effect of the transmission near the bistability edges. In the experimental data, the jumps of the optical states are not abrupt as expected, but follow the photodetector response lifetime ($\approx$ 6 ms).

In the thermo-optic bistability, the optical resonator intracavity intensity is likely to switch stable state due to external perturbation such as e.g. noise or input field modulation. The switching time τ_s is given by the thermalization time of the resonator. Under sufficiently strong external modulation, the resonator can switch periodically, at the modulation frequency. However if the latter is higher than a certain cut-off frequency, given by $(2\tau_s)^{-1}$, the resonator cannot switch twice a modulation period. This cut-off frequency therefore defines a limitation for the processes relying of thermo-optic nonlinearity. In order to estimate the switching time τ_s, the input laser is modulated at sufficiently low-frequency for the transition regime to be observed. For this purpose, the laser wavelength is set at the center of the bistability ($\lambda = 1566.75$ nm) and modulated in the MZM with a square signal carrying amplitude $V_{\mathrm{mod}} = 2$ V and frequency $\omega_{\mathrm{mod}} = 2\pi \times 10$ kHz. At the waveguide output, a fiber splitter allows to trigger the transmitted signal via a fW sensitive photodetector.

Using a modulation depth $d = 0.89$ and frequency $\Omega_{\mathrm{mod}} = 2\pi \times 10$ kHz, we record the optical output and average hundreds of modulation periods. The data is shown in Fig. 1(c). Here, the optical resonator intra-cavity field switches from the cold state (high transmission) to the hot state and then returns back to the cold state at half a cycle following an exponential decay. We fit the data with a function $f(t) = A\exp(-t/\tau_s) + B$ which provides the thermalization time $\tau_s \approx 4.4$ μs. Following the above discussion, we deduce that the corresponding cut-off frequency $\omega_{\text{cut-off}} = \gamma_{\mathrm{th}} = 2\pi \times 113.6$ kHz.

In addition to the change of the refractive index, light absorption induced temperature changes also affect the elastic properties of InP. In particular, all elastic moduli—Young's modulus, bulk modulus, and shear modulus—decrease with rising temperature [2] and consequently makes heated InP material easier to compress. This change of the elastic moduli can be experimentally probed by a change of the mechanical frequency for increasing photon absorption. The heatmap in Fig. 2 shows the power spectral density of the optical output for varying detuning Δ with $P_{\mathrm{in}} = 325\mu$W. As the detuning is swept towards resonance $(\Delta = 0)$, the cavity will host more photons and hence maximize their absorption by the cavity. This will result in maximal temperature at resonance and Fig. 2 shows that mechanical frequency is minimal in accordance with the material's softening. The heating of InP material related to photon absorption takes place in the thermal modes [3, SI p. 13] within the L3 defect cavities and thus in a very localised manner. Noting that the InP material forming the cavity can only expand freely in the direction perpendicular to the membrane illustrated in Fig. 1(a) of the main text. Any expansion of the heated InP material within the remaining two dimensions will cause stress onto the surrounding InP material in the photonic crystal. By virtue of Newton's laws, the surrounding material will hence react with stress onto the L3 defects for any expansion that is not normal to the membrane. In summary, stress that is caused by the suspension of the cavity upon expansion in combination with the softening of the material under heating can overcome thermal expansion for a sufficiently large temperature gradient. This can lead to an overall red-shift of the cavity resonance as depicted in Fig. 1 even though the *differential cavity shift at the work point* g_T can be a blue-shift $(g_T > 0)$. In general, the differential cavity shift $g_T = \partial\omega_{\rm op}/\partial T$ is a smooth function of temperature and can change sign according to the softening mechanism. From room temperature to an intermediate temperature where the stress caused by the suspension of the cavity overcomes the stress by thermal expansion, the cavity will accumulate a red-shift. If this shift is larger than the accumulated blue-shift from the intermediate to the final temperature, it will result in an overall red-shift of the cavity resonance even though the differential cavity shift at the final temperature $(g_{\rm T} g_{\rm abs}/\gamma_{\rm th} > 0)$ is a blue-shift.

Additionally, Fig. 2 illustrates that the mechanical frequency undergoes a noticable shift of 80 kHz on optical resonance which could also be attributed to optomechanical or photothermal backaction. Employing the optical linewidths, the mechanical frequency and the dispersive optomechanical coupling, the theory $\Omega_j'(\Omega_j)$ predicts a shift below 1 Hz which is nearly four orders of magnitude below the shift observed in the setup. Moreover, the mechanical linewidth Γ extracted for the fits is constant with the detuning. This is an indication that dynamical backaction is negligible in this optomechanical system and can also be used to outrule photothermal backaction as summarized in Eq. (7) of [4]. Employing the change of the mechanical linewidth resulting from the photothermal elastic backaction effect $\Gamma_{\rm eff} = \Gamma_1(1+\delta\Gamma/\Gamma_1) = \Gamma_1\{1+[\tau_{\rm th}/(1+\Omega_1^2\tau_{\rm th}^2)]\times(2\beta R/mc\Gamma_1)({\rm d}P_{\rm Abs}/{\rm d}x)\}$ allows us to set a boundary to the second summand. This summand describes the relative change of the linewidth which is limited by the measurement imprecision in our experiment. For the purpose of giving an upper limit on the expected frequency shift, the relative imprecision of the linewidth can be set to unity even though it is below 10 % in the concrete case of Fig. 2. This allows to estimate the expected frequency shift $\Omega_{\rm eff}^2 = \Omega_1^2[1-(\delta\Gamma/\Gamma_1)\times(\Gamma_1/\Omega_1^2\tau_{\rm th})]$ according to photothermal backaction [4]. With the upper boundary of relative uncertainty in linewidth of unity the frequency shift amounts to $\Delta\Omega = \Omega_1 - \Omega_{\rm eff} = \Omega_1[1-(1-\Gamma_1\tau_{\rm th}^{-1}/\Omega_1^2)^{1/2}]$. Employing $\tau_{\rm th} = \tau_s$ along with the mechanical frequency and linewidth predicts a frequency shift lower than 80 Hz based on photothermal backaction and thus three orders of magnitude lower than the observed frequency shift in Fig. 2. In summary, ruling out dynamical backaction indicates that this frequency shift originates in a thermo-mechanical effect as the above discussed softening mechanism.

III. MODULATION DEPTH INFLUENCE

We record the noise spectrum while varying the modulation voltage from 0 to 2 V. The heatmap shown in Fig. 3 evidence the progressive apparition of two pairs of sidebands around the mechanical resonance ($\Omega_1 = 2\pi\times 4.340$ MHz). The sidebands start to display imbalance amplitudes around $d = 0.75$. The thermo-optically induced imbalance of the modulation sidebands for large modulation depths can be employed for an amplification of the Floquet mechanism. Eq. (8) of the main text implies that an increase of the sideband amplitudes leads to an increased coupling of the Floquet mechanism. We therefore explore the dependence of the amplitude numerically. We employ the same parameters as in Fig. 2 (c) of the main text except for an even larger modulation depth $d = 2.0$. These parameters lead to an inverted sideband imbalance as displayed in Fig. 4. In contrast to the large modulation frequency case, the positive sideband is increased for low modulation frequencies. We therefore find the surprising result that thermo-optical effects can be used to suppress and to amplify the coupling strength that enables the Floquet control.

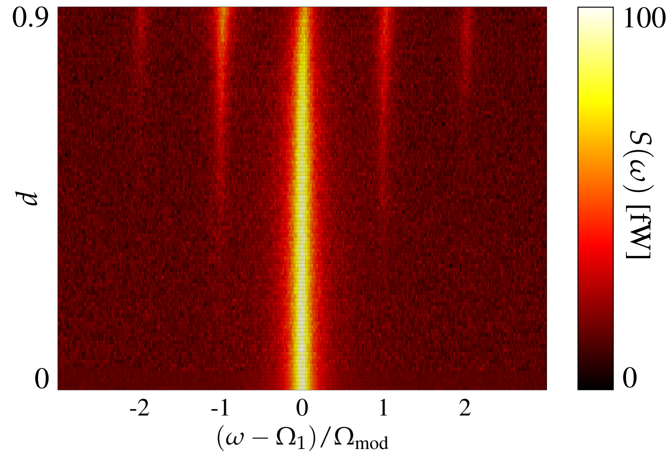

FIG. 3. Experimental record of the power spectral density for $P_{\rm in} = 1.3$ mW as a function the modulation depth showing the appearance of the first pair of sidebands around $d = 0.45$ and the appearance of the second pair around $d = 0.75$ and an imbalance in the amplitude of the first pair of sidebands (with $\Omega_{\rm mod} = 2\pi\times 50$ kHz).

IV. NUMERICAL SIMULATION PROCEDURES DEMONSTRATING BISTABILITY CONTROL

The numerical procedure that we use to generate the sample trajectories of our model displayed in Fig. 3 (b) of the main text employs the Euler–Maruyama scheme [1] for the dynamics of the mean fields

$$\dot{\alpha} = \left\{-i\left[\Delta - \sum_{j=1}^{N} g_j {\rm R}(\beta_j)\right] - \frac{\kappa}{2}\right\}\alpha + \mathcal{E}_0\mathcal{T}e^{-i\phi_0} + \xi_\alpha(t),$$
$$\dot{\beta}_j = -\left(i\Omega_j + \frac{\Gamma_j}{2}\right)\beta_j + ig_j|\alpha|^2 + \xi_{\beta_j}(t), \tag{5}$$

where we choose the parameters of the two mechanical modes ($N = 2$) as described in the main text, namely $\Omega_1 = 2\pi\times 10$ MHz, $\Gamma_1/\Omega_1 = 0.1$, $g_1 = 2\pi\times 151.630$ Hz (exact numerical value: 952.717 Hz), $\Omega_2 = 2\pi\times 11$ MHz, $\Gamma_2/\Omega_2 =$

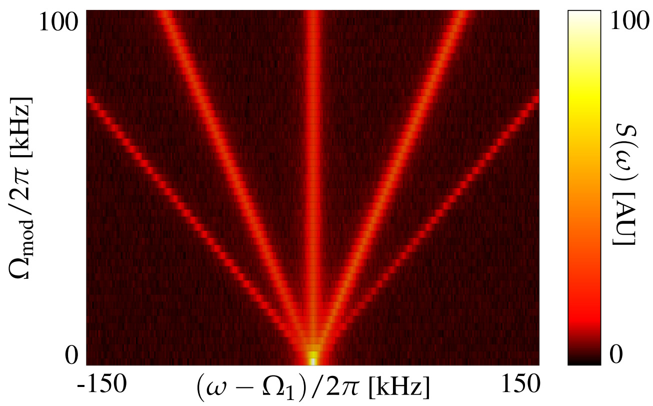

FIG. 4. Numerical evidence of the inversion of the sideband imbalance for low modulation frequencies with modulation depth $d = 2.0$. The increased amplitude of the first positive sideband proves that the thermo-optical effect can suppress or amplify the Floquet control mechanism.

10^{-2}, $g_2 = 2\pi \times 8.390$ Hz (exact numerical value: 52.717 Hz) as well as the optical cavity $\Delta = 2\pi \times 26.200$ MHz (exact numerical value: 164.619 MHz), and $\kappa = 2\pi \times 14.038$ MHz (exact numerical value: 88.0211 MHz). This places the numerical example in the unresolved sideband regime. The Gaussian noise terms we employ are described by their statistical momenta, i.e. their mean $\langle \xi_s(t) \rangle = 0$ taken to be zero thoughout the analysis and time correlation $\langle \xi_r(t)\xi_s(t') \rangle = \delta_{rs}\lambda_s\delta(t - t')$ for all $2(N+1)$ variables r and s denoting the real $\mathrm{Re}(z) = \mathrm{R}(z)/2$ and imaginary $\mathrm{Im}(z) = \mathrm{I}(z)/2$ parts of α and β_j with the variance of the Gaussian noise λ_s gauging the strength of the random forces. Throughout our simulations we employ $\lambda_{\mathrm{Re}(\alpha)} = \lambda_{\mathrm{Im}(\alpha)} = 1$ mimicking cavity shot noise as well as noise consistent with the zero point fluctuations of β_1, described by $\lambda_{\mathrm{Re}(\beta_1)} = \lambda_{\mathrm{Im}(\beta_1)} = 1$. The noise in the control oscillator is parametrized by $\lambda_{\mathrm{Re}(\beta_1)} = \lambda_{\mathrm{Im}(\beta_1)} = 8001$. We generate an initial condition of the system at the end of the bistable region by evolving the system without noise starting from rest $\alpha(t = -2t_0) = \beta_j(t = -2t_0) = 0$ for $t_0 = 50$ μs and constant drive with $\mathcal{E}_0 = 2\pi \times 1449427.676$ MHz (exact numerical value: 9107022.675 MHz), $\mathcal{T}_0 = (1-i)/2$, $\phi_0 = 0$. To generate realistic initial conditions, we then repeat the procedure with noise for another $t_0 = 50$ μs. After the initial procedure to approach the bistability edge of the system, we then drive with $\mathcal{T}_0 = (1 - i\mathcal{J}_0(d))/2$, $\mathcal{T}_{\pm 1} = -\mathcal{J}_1(d)$ and switch on the intensity modulation with $d = 1.875 \times 10^{-5}$ for $t = 200$ μs. After the modulation has been probed we evolve the system without modulation for another 50 μs to make sure that simulations that were changing steady state have sufficient time to converge and surpass our switching criterion. The bistable state we start from is characterized by a mean number of quanta of β_1 around 46500 whereas the other state is sustains approximately 79000 oscillator quanta. Thus, switching occurs if the mechanical oscillator quanta of β_1 surpass 60000 at the end of the simulation. The step size $\delta t = 0.0001\mu s$ throughout every simulation in order to numerically converge. We conducted 50 such runs for modulation with $\Omega_{\mathrm{mod}} = 2\pi \times 1$ MHz which showed no switching event and another 50 runs with $\Omega_{\mathrm{mod}} = 2\pi \times 11$ MHz which showed two switching events. This result coincides with the analytic result that intensity modulation at the frequency of the control oscillator at $\Omega_2 = 2\pi \times 11$ MHz is resonant and can lead to switching whereas off-resonant optical modulation does not affect the bistable state of $\hat{b}_1$. We conducted another set of deterministic simulations of

$$\dot{\alpha} = \left\{ -i\left[\Delta - \sum_{j=1}^{N} g_j \mathrm{R}(\beta_j)\right] - \frac{\kappa}{2} \right\}\alpha + \mathcal{E}_0\mathcal{T},$$

$$\dot{\beta}_j = -\left(i\Omega_j + \frac{\Gamma_j}{2}\right)\beta_j + ig_j|\alpha|^2 + iD\cos(\omega t + \phi_2), \quad (6)$$

with $\mathcal{E}_0 = 2\pi \times 1449428.344$ MHz (exact numerical value: 9107026.875 MHz), $D = 2\pi \times 246.69$ MHz (exact numerical value: 1550 MHz), $d = 10^{-4}$ and the system parameters used in the prior simulation. The numerical procedure consists of the initialization process from rest to the parameters at the bistability edge for $t_0 = 50$ μs with $D = 2\pi \times 0$ MHz followed by a simulation for 500 μs for the respective phase ϕ_2 and Ω_{mod}. The threshold criterion is equivalent to discriminating the steady states by the mean photon number $|\alpha|^2$. Fig 3 (b) of the main text shows that one steady state is characterized by a mean photon number of 3×10^9 and the other steady state attains a mean photon number of 5×10^9. Thus our discrimination criterion is to attribute a photon number smaller than 4×10^9 after the evolution protocol to the initial steady state and a photon number larger than 4×10^9 to a switching event leading to the phase diagram of Fig. 3 (c) in the main text. The time requirements of the numerical algorithm limit the maximal simulation time per data point leading to fluctuations in the phase diagram because the respective simulations are undergoing the transition but are still below the threshold.

[1] P. E. Kloeden and E. Platen, *Numerical Solution of Stochastic Differential Equations* (Springer-Verlag, Berlin-Heidelberg, 1992).

[2] P. S. Branicio, J. P. Rino, C. K. Gan, and H. Tsuzuki, J. Phys.: Condens. Matter **5**, 095002 (2009).

[3] E. Verhagen, S. Deléglise, S. Weis, A. Schliesser, and T. J. Kippenberg, Nature **482**, 63 (2012).

[4] J. Restrepo, J. Gabelli, C. Ciuti, and I. Favero, C. R. Phys. **12**, 860 (2011).